Appl Phys A (2011) 102: 909–914
DOI 10.1007/s00339-011-6272-9

Applied Physics A
Materials Science & Processing

Multiscale simulation on electromigration of the oxygen vacancies in metal oxides

Sang Ho Jeon · Won-Joon Son · Bae Ho Park · Seungwu Han

Received: 30 September 2010 / Accepted: 22 December 2010 / Published online: 21 January 2011

Abstract The energetics and dynamics of electromigration of the oxygen vacancy is investigated with first-principles calculations and kinetic Monte Carlo methods. To simulate the charged oxygen vacancy under external fields within the first-principles approach, we introduce a slab model with electron-accepting dopants in the surface. The analysis of the density of states confirms that the oxygen vacancies are positively charged. When the external field is applied, the total energy of the slab linearly changes with respect to the position of the charged vacancy in the field direction, which allows for probing local permittivity around the vacancy site. The activation energy of vacancy migration is lowered along the field direction in a manner that the charge state of the vacancy is maintained along the migration path. Kinetic Monte Carlo simulations based on the first-principles inputs are also carried out and it is shown that the high-temperature condition is important for the fast redistribution of charged vacancies.

1 Introduction

The material properties of metal oxides, especially electrical properties, critically depend on the presence of lattice imperfections such as the grain boundary and point defects. In particular, the oxygen vacancy (V_O), which constitutes a most fundamental point defect in oxides, plays crucial roles in the performance of various electronic devices that include oxide materials. As a traditional example, the fatigue phenomena in ferroelectric memories have been understood based on the movement of V_O driven by electrical fields [1]. In the metal-oxide-semiconductor field effect transistor (MOSFET), high dielectric-constant materials such as HfO_2 are now replacing the traditional silicon oxides. To enhance the device performance, the high-work function metal gates are used in pair with HfO_2 in p-type MOSFET [2]. However, it is observed that effective work functions of metal gates shift to lower values after thermal annealing [3]. It has been strongly evidenced that the creation and diffusion of the charged V_O during the annealing process play a significant role [3–6]. More recently, V_O has been receiving renewed attentions owing to its role in the resistance-switching random access memory (RRAM) [7, 8]. In short, the operation of RRAM is based on the soft-breakdown of oxides which can be controlled by applying the bias. The microscopic origin of RRAM is still contentious, but it is widely accepted that the electromigration of the charged V_O is crucial for the formation and rupture of the local conducting path [9–11]. Therefore, in several electronic devices, it is crucial to understand how the charged V_O drifts under the electrical bias.

Classically, the charged V_O can be regarded as a point particle with the fixed charge moving with a certain activation energy, which is also supported by a rigorous approach [12]. However, to take into account various local environments more realistically, it would be desirable to simulate the charged V_O under the electrical bias directly within the first-principles framework. As far as we are aware, there has been no attempt to apply the first-principles method to study the charged V_O in the presence of electric fields. This is in part because V_O responds to the electric field only when it is positively or negatively charged. The charged defects are considered typically by adjusting the electron numbers per

S.H. Jeon · W.-J. Son · S. Han (✉)
Department of Materials Science and Engineering, Seoul National University, Seoul 151-744, Korea
e-mail: hansw@snu.ac.kr

B.H. Park
Department of Physics, Konkuk University, Seoul 143-701, Korea

unit cell. Within the periodic boundary conditions used in the plane-wave formalism, the background charge is introduced to eliminate the divergence in the electrostatic energy. However, the electric dipole in such a system is ill-defined since the center of the uniform charge is not unique. This gives rise to a problem when the external field is applied; in the presence of the uniform electric field (E_{ext}), the total energy (E_{tot}) is written as follows [13]:

$$E_{\text{tot}} = E_{\text{tot}}^{\text{KS}} - E_{\text{ext}} \cdot P, \tag{1}$$

where $E_{\text{tot}}^{\text{KS}}$ is the usual energy functional in the absence of the external bias and P is the polarization along the field direction. Since P is not well defined in a system with the uniform background charge, the total energy formalism is not valid any more.

In this work, the above technical problem is resolved by introducing charge-accepting dopants in the model system. Our first-principles results show that the charged V_{O} can be reasonably described as a charged point particle possessing the nominal charge of V_{O}. The present approach also provides a new way to probe the local dielectric constant. Based on the first-principles inputs, we also carry out the kinetic Monte Carlo simulations on the nanoscale capacitor to investigate the redistribution of V_{O} over realistic time scales.

2 Computational methods and model systems

We carry out the density functional calculations within the local density approximation [14] for MgO, SrO, and α-Al_2O_3, three representative oxide materials. The computational package of VASP [15, 16] is used throughout this work. We use projector-augmented-wave potentials [17] for describing electron–ion interactions. The cut-off energy for the plane-wave basis is set to 500 eV. For k-point sampling, $2 \times 2 \times 1$ meshes are used for the slab structures. Further increase of k-points changes the total energy less than 0.1 meV/atom. For all calculations, we relax ionic positions until atomic forces are reduced to within 0.03 eV/Å. For the bulk phase, it is found that the lattice parameters agree with the experiment within 2%. In order to simulate V_{O} under the influence of the external electric field (E_{ext}), we consider model slabs as shown in Fig. 1. The surface direction of the slab geometry (z-direction) are chosen to be (001) and (0001) for MgO (SrO) and Al_2O_3, respectively, and external fields are applied along the surface normal. The slab thickness is selected such that the dielectric constant in the middle region recovers the bulk value (see below). The oxygen vacancy is introduced in one of the three layers ($L_{\text{C}-1}$, L_{C}, and $L_{\text{C}+1}$) in the middle part of the slab (see Fig. 1). The lateral dimensions in the xy-plane are expanded to minimize the interactions between vacancies in neighboring cells. (The nearest-neighbor distances between V_{O}'s are 10, 12, and

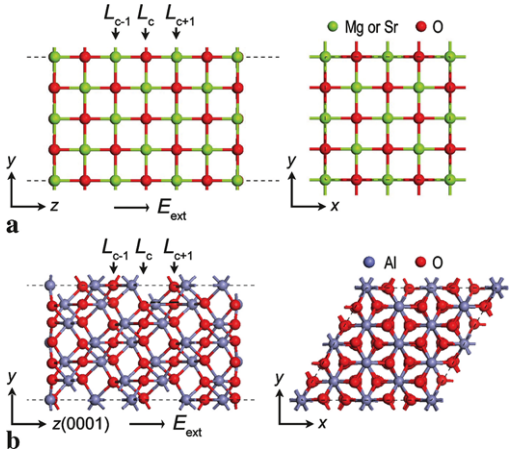

Fig. 1 The unit cell of model slabs. (**a**) MgO or SrO, and (**b**) α-Al_2O_3

13 Å for MgO, SrO, and Al_2O_3, respectively.) The repeated slabs along the z-direction are separated by the vacuum by 10 Å, which is long enough to avoid wave function overlap between slabs. The external field is applied with a sawtooth potential that is compatible with periodic boundary conditions. To cancel the induced dipole fields from other slabs, a compensating dipole layer is introduced in the middle of the vacuum region [18].

As discussed in the introduction, V_{O} responds to the electric field only when it is positively or negatively charged but the introduction of uniform charge is not compatible with the total energy formalism. We resolve this problem by introducing the electron-accepting dopant in the slab surface. For example, if one of the Mg sites in both surfaces of the MgO slab is replaced by the monovalent Li atom, two electrons trapped in the vacancy site fall into the acceptor site, leaving behind the doubly ionized V_{O}^{+2}. Similarly, Na and Be atoms are adopted in SrO and Al_2O_3 slabs. From the analysis on the density of state (DOS), it is confirmed that the dopants chemically affect only neighboring oxygen atoms. However, the electrostatic interaction between the charged dopants and V_{O}^{+2} is significant. To remove this from the computational results, we focus on the differences in various physical quantities between with and without external biases.

3 Results and discussions

3.1 Model slabs under the external field

We first examine on the effects of external fields on the model slab without vacancies or dopants. The external field redistributes electrons and ions, which gives rise to the change in the electrostatic potential. It is convenient to de-

fine the planar-averaged potential $\Delta V(z)$ as follows:

$$\Delta V(z) = \frac{1}{A}\int_A \big[V_{\mathrm{loc}}(x, y, z; E_{\mathrm{ext}}) - V_{\mathrm{loc}}(x, y, z; 0)\big]\, dx\, dy, \quad (2)$$

where A is the area of the surface unit cell in the xy-plane, and $V_{\mathrm{loc}}(x, y, z; E_{\mathrm{ext}})$ is the sum of ionic and Hartree potentials under the external field of E_{ext}. To smear out the atomic-scale oscillations, the macroscopic average is performed [19]:

$$\Delta\overline{V}(z) = \frac{1}{l}\int_{z-l/2}^{z+l/2} \Delta V(z')\, dz', \quad (3)$$

where l is the length of bulk periodicity along the field direction. Figure 2 shows $\Delta\overline{V}(z)$ for each slab when E_{ext} of 0.5 V/Å is applied. The magnitude of the external field is confirmed by the potential slope in the vacuum. It is noticeable that the slope of $\Delta\overline{V}(z)$ is significantly reduced inside the slab, which essentially represents the dielectric response of the system. From the inverse ratio of the slope of $\Delta\overline{V}(z)$ to E_{ext}, the local static permittivity $[\varepsilon^0(z)]$ can be obtained:

$$\varepsilon^0(z) = -E_{\mathrm{ext}} \Big/ \frac{d}{dz}\Delta\overline{V}(z). \quad (4)$$

The dashed lines in Fig. 2 indicate $\varepsilon^0(z)$. It is found that $\varepsilon^0(z)$ is enhanced near the surface region. This could be attributed to the weakened bonding in the surface region. A similar observation was also found in Ref. [20]. The bulk dielectric constant corresponds to the value in the middle of each slab. This is summarized in Table 1. For comparison, the experimental data ($\varepsilon^0_{\mathrm{exp}}$) and the theoretical value in the crystalline structure ($\varepsilon^0_{\mathrm{bulk}}$) are also displayed. The theoretical values were calculated within the density functional perturbation formalism [23]. The agreements between these three values are satisfactory, except for SrO for which the theoretical values are significantly larger than the experimental data.

3.2 Oxygen vacancies under external fields

Next, we introduce V_{O} in one of the three middle layers ($L_{\mathrm{C}-1}$, L_{C}, and $L_{\mathrm{C}+1}$) and calculate the energy difference ΔE defined as follows:

$$\Delta E = E_{\mathrm{tot}}(0.5\ \mathrm{V/Å}) - E_{\mathrm{tot}}(0\ \mathrm{V/Å}), \quad (5)$$

where $E_{\mathrm{tot}}(E_{\mathrm{ext}})$ is the total energy under the external field of E_{ext}.

In the absence of electron-accepting dopants, the oxygen vacancy remains neutral, and ΔE among the three layers change by less than 0.05 eV. This is because the neutral vacancy does not respond to the external field. However, when the dopants are introduced in the surface layer, we find that the oxygen vacancy is doubly ionized (V_{O}^{+2}). This is confirmed by examining DOS, which showed that the defect levels associated with V_{O} lie above the Fermi level, and therefore are empty.

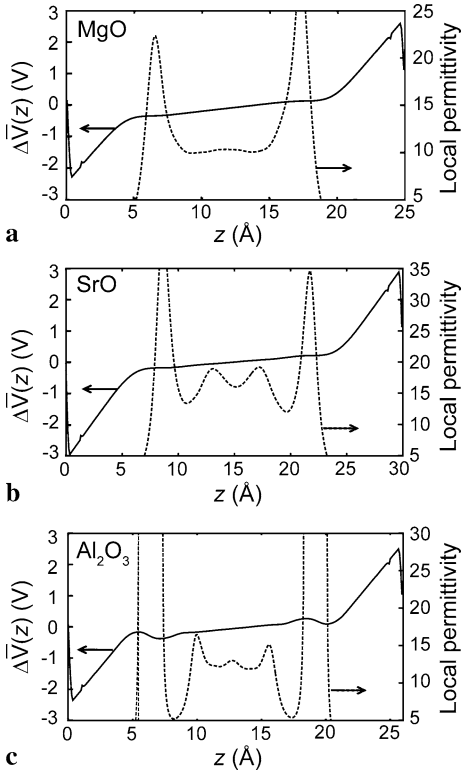

Fig. 2 The macroscopically averaged potential differences (*solid lines*) and the local permittivity (*dashed lines*). (**a**) MgO, (**b**) SrO, and (**c**) α-Al_2O_3

Table 1 The dielectric constant of each metal oxide

	$\varepsilon^0_{\mathrm{slab}}$	$\varepsilon^0_{\mathrm{bulk}}$	$\varepsilon^0_{\mathrm{exp}}$	$\varepsilon^0_{\mathrm{relaxed}}$	$\varepsilon^0_{\mathrm{fixed}}$
MgO	10.16	10.72	9.65[a]	12.06	11.92
SrO	17.47	17.85	13.3[a]	18.64	20.45
α-Al_2O_3	12.67	11.01	9.63[b]	12.02	11.73

[a]Ref. [21]

[b]Ref. [22]

Figure 3(a) shows ΔE with respect to the position of V_{O}^{+2} in the middle layers. As expected, ΔE changes linearly with respect to the position of V_{O}. Theoretically, when V_{O}^{+2} moves from $L_{\mathrm{C}-1}$ to L_{C} or from L_{C} to $L_{\mathrm{C}+1}$, ΔE should drop by $\Delta\Delta E$ defined as follows [12]:

$$\Delta\Delta E = \frac{2|e|E_{\mathrm{ext}}d}{\varepsilon^0}, \quad (6)$$

where ε^0 is the static dielectric constant at the position of V_{O}^{+2} and d is the interlayer spacing. By rearranging terms,

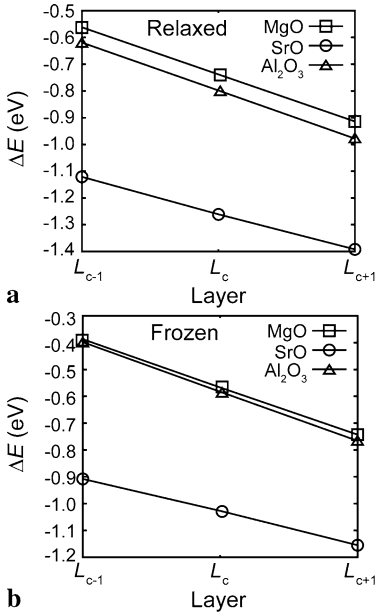

Fig. 3 The energy variation with respect to the vacancy position in different layers. In (**a**), the atomic positions are fully relaxed, while the atoms in (**b**) are frozen to those without external fields

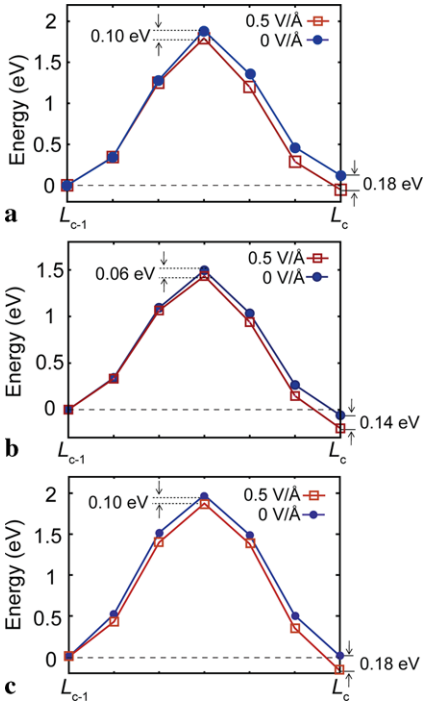

Fig. 4 The potential profile for the charged vacancy migrating from L_{C-1} to L_C layers. (**a**) MgO, (**b**) SrO, and (**c**) α-Al_2O_3

one can obtain the local permittivity at the site of the vacancy as follows:

$$\varepsilon^0 = \frac{2|e|E_{\text{ext}}d}{\Delta\Delta E}. \tag{7}$$

The $\varepsilon^0_{\text{relaxed}}$ in Table 1 shows the values of ε^0 that follow from (7) and $\Delta\Delta E$ in Fig. 3(a). It is found that they are in good agreement with $\varepsilon^0_{\text{slab}}$ or $\varepsilon^0_{\text{bulk}}$. This suggests that the energy change as the charged vacancy move around a specific position can be used to evaluate the local permittivity at that position. For example, this approach can be employed in studying the variation of dielectric constant near the interface [24, 25]. Compared to the previous approaches [24, 25], the present scheme works even when the interface is laterally irregular because the oxygen vacancy is spatially localized in three dimensions.

We also consider the case where the ionic positions are fixed to those optimized without external fields. This was motivated by the possibility of calculating the optical dielectric constant (ε^∞), since the lattice components of the dielectric response are excluded. The results are shown in the last column of Table 1 ($\varepsilon^0_{\text{fixed}}$). Surprisingly, $\varepsilon^0_{\text{fixed}}$ nearly reproduces the static dielectric constants. For comparison, ε^∞ for MgO, SrO, and Al_2O_3 are 3.20, 3.91, and 3.17, respectively [21, 26]. This means that the ionic relaxation energies under the external field are similar regardless of the vacancy position. However, these counterintuitive results are rather difficult to rationalize at this moment. This result also implies that the local permittivity can be calculated without atomic relaxation under the external field, which can significantly reduce the computational cost.

One important quantity for the dynamics of the oxygen vacancy is the activation energy for the vacancy migration. The external field induces the asymmetry in the migration barrier along the field direction, which leads to the non-uniform distribution of the oxygen vacancy. To investigate this in more detail, we study the migration barrier of the charged V_O under the external field by applying the nudged-elastic band (NEB) method [27]. Five equally-spaced replicas are considered to describe the migration path between L_{C-1} and L_C layers and the results are shown in Fig. 4. The migration barriers in the absence of external fields are 1.83, 1.5, and 2.0 eV for MgO, SrO, and Al_2O_3, respectively. These values are much smaller than for the neutral vacancies since the electrons trapped in the neutral vacancy give rise to significant strain energies at the saddle point. When the external field of 0.5 V/Å is applied, the energy barrier in the forward direction is lowered by ΔE_a as noted in each figure. It can be seen that ΔE_a is very close to the half of ΔE, the lowered energy when V_O arrives at L_C. This is because transition states in these oxides are halfway between the oxygen layers. The present result also indicates that the nominal charge of V_O is maintained to be $+2e$ during the migration process.

3.3 Kinetic Monte Carlo simulations

In electronic devices such as RRAM, the vacancy distribution is controlled by the bias application, and it is important to estimate the time scale required for invoking macroscopic redistribution of vacancies. This cannot be simulated directly by the first-principles methods because the system size and the time scale are far beyond the current computational capability. Instead, we employ the kinetic Monte Carlo (KMC) method by considering the vacancy dynamics in a simplified way. Specifically, it is assumed that the oxygen sublattice forms a simple cubic structure and oxygen diffuses only through the oxygen-vacancy exchange mechanism. The hopping rate (ν) between jumps is obtained from the following Boltzmann relationship:

$$\nu = \nu^* \exp\left(-\frac{E_a}{kT}\right), \tag{8}$$

where k and T are Boltzmann constant and temperature, respectively, and E_a is the migration barrier along the jump direction. The magnitude of E_a and its variation along the field direction are obtained from the above first-principles calculations. The attempt frequency (ν^*) in (8) can be evaluated within the harmonic transition-state theory (HTST) [28], which is a good approximation for solid-state systems;

$$\nu^* = \frac{(\prod_{j=1}^{3N} \nu_j)_{\text{minimum}}}{(\prod_{j=1}^{3N-1} \nu_j)_{\text{saddle}}}, \tag{9}$$

where the numerator is the product of phonon modes in the equilibrium state and the denominator is that at the saddle point excluding one unstable component along the migration path. We calculate ν^* from the bulk calculation at zero external field. The phonon frequencies can be obtained by diagonalizing the dynamical matrix.

For the specific material parameters, we employ MgO. The migration barrier is then 1.83 eV from Fig. 4(a) and ν^* from HTST is 13 THz. The lattice spacing in the oxygen sublattice is set to 2.83 Å, which is the distance between nearest-neighboring O atoms in MgO. The $51 \times 51 \times 35$ grid points are selected in xyz dimensions with the electrodes normal to the z-axis (see Fig. 5(a)) and the periodic boundary conditions are used in the xy-plane. The vacancy concentration is assumed to be 1% or 910 vacancies in the unit simulation box. For the KMC simulations, we adopt a simple residence-time algorithm [29]. For random number generation, a generalized feedback shift register, R250, is used [30]. For simplicity, we consider only the movement to the nearest-neighbor positions, and the interaction between vacancies is not considered.

Figure 5(a) shows the schematic diagram of the simulation cell. In the initial stage, V_O's are randomly distributed throughout the insulator. When the external bias is applied, the positively charged V_O's are attracted to the cathode side as depicted in the right figure of Fig. 5(a). One typical example of the temporal sequence of the vacancy distribution is shown in Fig. 5(b), assuming an electric field of 0.3 V/nm and a temperature of 600 K. To assign the characteristic response time, we define the "set time" (τ_s) as the minimum time required for accumulating 90% of vacancies within the 0.5 nm within the cathode-insulator interface. Such an accumulation of V_O can induce the lowering of the Schottky barrier at the interface [9, 31, 32]. The results with various temperatures and electric fields are presented in Fig. 5(c). It is found that τ_s is very long at the room temperature ($T = 300$ K). Even with an electric field as high as 1 V/nm, which is close to the field emission condition, τ_s is ~300 years. However, if the temperature is increased to 600 K or 900 K, τ_s is greatly shortened such that the response time is in the range of the practical elec-

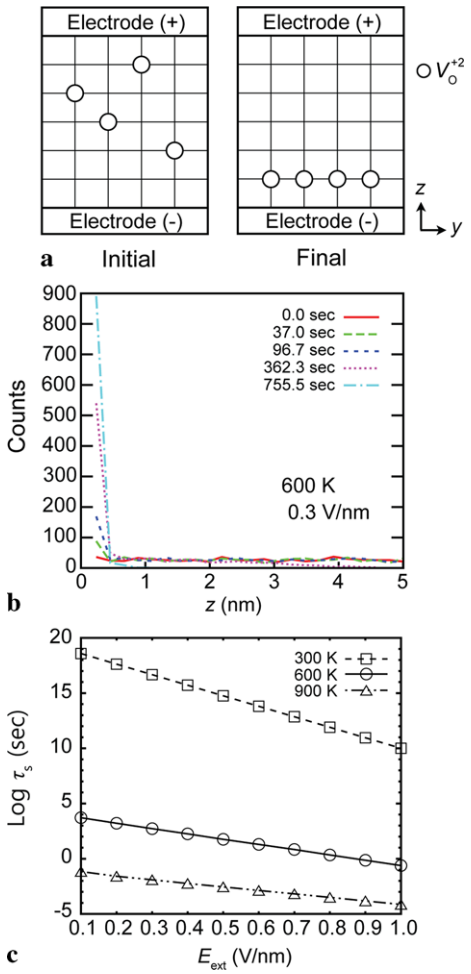

Fig. 5 (**a**) Schematic diagram to show the initial and final geometries in kinetic Monte Carlo simulations. (**b**) The distribution of the oxygen vacancy along the field direction with respect to time. The field is applied at zero time. The numbers are summed over the xy-plane. (**c**) The set time (τ_s) at various temperatures is shown as a function of the external field

tronic devices. Therefore, it is demonstrated that the high-temperature condition is critical for the fast redistribution of oxygen vacancies in metal oxides. This result is in line with the experimental observation that the Joule heating is important for resistance switching in RRAM [33, 34].

4 Conclusion

In conclusion, we have proposed a first-principles approach to directly simulate the charged V_O under the external field. The oxygen vacancies could be charged by introducing the electron-accepting dopants in the slab surface. The energy variation with respect to the vacancy position could be exploited as an effective local "dielectric-constant meter". The KMC simulations based on the first-principles input was carried out and it was revealed that the high-temperature condition is important for the fast redistribution of charged vacancies. The present work demonstrates that multiscale simulation of charged vacancies under the electric field is feasible by combining the first-principles approach and the KMC methods.

Acknowledgements This work was supported by Quantum Metamaterials Research Center (Grant No. R11-2008-053-03001-0). The computations were carried out at KISTI Supercomputing Center (KSC-2010-C2-0010).

References

1. M. Dawber, J.F. Scott, Integrated. Ferroelectrics **32**, 259 (2001)
2. B.H. Lee, J. Oh, H.H. Tseng, R. Jammy, H. Huff, Mater. Today **9**, 32 (2006)
3. E.P. Gusev, V. Narayanan, M.M. Frank, IBM J. Res. Dev. **50**, 387 (2006)
4. S. Guha, V. Narayanan, Phys. Rev. Lett. **98**, 196101 (2007)
5. E. Cho, B. Lee, C.-K. Lee, S. Han, S.H. Jeon, B.H. Park, Y.-S. Kim, Appl. Phys. Lett. **92**, 233118 (2008)
6. J. Robertson, O. Sharia, A.A. Demkov, Appl. Phys. Lett. **91**, 132912 (2007)
7. R. Waser, M. Aono, Nat. Mater. **6**, 833 (2007)
8. A. Sawa, Mater. Today **11**, 28 (2008)
9. S.H. Jeon, B.H. Park, J. Lee, B. Lee, S. Han, Appl. Phys. Lett. **89**, 042904 (2006)
10. K. Szot, W. Speier, G. Bihlmayer, R. Waser, Nat. Mater. **5**, 312 (2006)
11. D. Kwon, K.M. Kim, J.H. Jang, J.M. Jeon, M.H. Lee, G.H. Kim, X. Li, G. Park, B. Lee, S. Han, M. Kim, C.S. Hwang, Nat. Nanotechnol. **456**, 148 (2010)
12. S.A. Prosandeev, J. Phys., Condens. Matter **14**, L745 (2002)
13. P. Umari, A. Pasquarello, Phys. Rev. Lett. **89**, 157602 (2002)
14. D.M. Ceperley, B.J. Alder, Phys. Rev. Lett. **45**, 566 (1980)
15. G. Kresse, J. Hafner, Phys. Rev. B **47**, 558 (1993)
16. G. Kresse, J. Hafner, Phys. Rev. B **49**, 14251 (1994)
17. P.E. Blöchl, Phys. Rev. B **50**, 17953 (1994)
18. L. Bengtsson, Phys. Rev. B **59**, 12301 (1999)
19. J. Junquera, M.H. Cohen, K.M. Rabe, J. Phys., Condens. Matter **19**, 213203 (2007)
20. L. Yu, V. Ranjan, M.B. Nardelli, J. Bernholc, Phys. Rev. B **80**, 165432 (2009)
21. A.A. Demkov, A. Navrotsky, *Materials Fundamentals of Gate Dielectrics* (Springer, Amsterdam, 2005)
22. A.K. Harman, S. Ninomiya, S. Adachi, J. Appl. Phys. **76**, 8032 (1994)
23. X. Gonze, C. Lee, Phys. Rev. B **55**, 10355 (1997)
24. M. Stengel, N.A. Spaldin, Nature **443**, 679 (2006)
25. B. Lee, C.-K. Lee, S. Han, J. Lee, C.S. Hwang, J. Appl. Phys. **103**, 024106 (2008)
26. C.-K. Lee, E. Cho, H. Lee, K. Seol, S. Han, Phys. Rev. B **76**, 245110 (2007)
27. G. Mills, H. Jonsson, G.K. Schenter, Surf. Sci. **324**, 305 (1995)
28. G.H. Vineyard, J. Phys. Chem. Solids **3**, 121 (1957)
29. R. Krishnamurthy, Y.G. Yoon, D.J. Srolovitz, R. Car, J. Am. Ceram. Soc. **87**, 1821 (2004)
30. S. Kirkpatrick, E.P. Stoll, J. Comput. Phys. **40**, 517 (1981)
31. J.J. Yang, M.D. Pickett, X. Li, D.A.A. Ohlberg, D.R. Stewart, R.S. Williams, Nat. Nanotechnol. **3**, 429 (2008)
32. T. Fujii, M. Kawasaki, A. Sawa, H. Akoh, Y. Kawazoe, Y. Tokura, Appl. Phys. Lett. **86**, 012107 (2005)
33. U. Russo, D. Ielmini, C. Cagli, A.L. Lacaita, IEEE Trans. Electron Devices **56**, 186 (2009)
34. J. Borghetti, D.B. Strukow, M.D. Pickett, J.J. Yang, D.R. Stewart, R.S. William, J. Appl. Phys. **106**, 124504 (2009)